The Bending Strip Method for Isogeometric Analysis of Kirchhoff-Love Shell Structures Comprised of Multiple Patches

J. Kiendl[a,*], Y. Bazilevs[b], M.-C. Hsu[b], R. Wüchner[a], K.-U. Bletzinger[a]

[a] *Lehrstuhl für Statik, Technische Universität München, Arcisstr. 21, München 80333, Germany*
[b] *Department of Structural Engineering, University of California, San Diego, La Jolla, CA 92093, USA*

Abstract

In this paper we present an isogeometric formulation for rotation-free thin shell analysis of structures comprised of multiple patches. The structural patches are C^1- or higher-order continuous in the interior, and are joined with C^0-continuity. The Kirchhoff-Love shell theory that relies on higher-order continuity of the basis functions is employed in the patch interior as in [1]. For the treatment of patch boundaries, a method is developed in which strips of fictitious material with unidirectional bending stiffness and zero membrane stiffness are added at patch interfaces. The direction of bending stiffness is chosen to be transverse to the patch interface. This choice leads to an approximate satisfaction of the appropriate kinematic constraints at patch interfaces without introducing additional stiffness to the shell structure. The attractive features of the method include simplicity of implementation and direct applicability to complex, multi-patch shell structures. The good performance of the bending strip method is demonstrated on a set of benchmark examples. Application to a wind turbine rotor subjected to realistic wind loads is also shown. Extension of the bending strip approach to the coupling of solids and shells is proposed and demonstrated numerically.

Keywords: isogeometric analysis, NURBS, rotation-free shells, Kirchhoff-Love theory, multiple patches, wind turbine rotor, shell-solid coupling

1. Introduction

Isogeometric Analysis was first proposed in [2] as a technology that has the potential to bridge the gap between design and analysis. Non-Uniform Rational B-Splines (NURBS) were employed as the first basis function technology in isogeometric analysis and is currently the most developed one. NURBS-based isogeometric analysis was applied with great success to the study of solids, structures,

*Corresponding author
Email address: kiendl@bv.tum (J. Kiendl)

fluids, fluid-structure interaction, turbulence, phase field modeling, and structural optimization [3–19]. Mathematical theory of NURBS-based isogeometric analysis was originally developed in [20]. Further refinements and insights into approximation properties of NURBS were studied in [21] using the concepts of Kolmogorov n-widths theory. Recent developments in isogeometric analysis include modeling and simulation of shell structures [1, 22, 23], coordinated synthesis of hierarchical engineering systems [24], isogeometric model quality assessment and improvement [25–27], applications to incompressible elasticity [28], and T-Splines [29, 30].

This article further develops the application of isogeometric analysis to shell structures that make use of the Kirchhoff-Love shell theory. The Kirchhoff-Love shell theory assumes that a cross section normal to the middle surface of the shell remains normal to the middle surface during the deformation, which implies that transverse shear strains are negligible. This theory is appropriate for thin shells ($20 \leq R/t$, where R is the shell radius of curvature and t is its thickness)[31]. Most shell structures of practical engineering interest satisfy this criterion. Thin shells have an optimal load-carrying behavior and therefore allow the construction of highly efficient light-weight structures [32, 33]. In the governing mechanical variational equations of the Kirchoff-Love theory, second order derivatives appear, and therefore C^1-continuity of the approximation functions is required for the discrete formulation to be conforming. NURBS basis functions have the necessary smoothness at the patch level. NURBS are inherently higher order, which also alleviates locking associated with low order shell discretizations. The attractive feature of the Kirchhoff-Love theory is that the formulation is purely displacement based and no rotational degrees of freedom are necessary [34–36].

In the previous works on rotation-free isogeometric shell analysis [1, 23], the authors showed that NURBS are able to attain very good accuracy and are efficient for shell structures. However, the developments were confined to single-patch shell structures, or a very limited class of multi-patch shell structures with simple linear constraints between control points to maintain a conforming discretization. In this paper, we propose a formulation that is rotation-free and is capable of handling a significantly larger class of structures composed of an arbitrary number of patches and their relative orientations. The method consists of adding strips of material in places where the NURBS patches are joined with C^0-continuity and has similarities with the "continuity patches" presented in [37]. The strips have bending stiffness only in the direction transverse to the patch intersection, and no membrane stiffness. These "bending" strips are generated automatically. They overlap one row of control points on each side of the patch intersection and prevent the structure from developing unphysical "kinks" at this location, which would occur otherwise. The methodology is able to handle patches that are coupled with G^1-continuity as well as patches that meet at a kink (e.g., the trailing edge of an airfoil). The method is simple to implement and its effectiveness and accuracy are shown using a variety of numerical examples.

The paper is outlined as follows. The governing equations of the Kirchhoff-

Love shell theory are presented in Section 2. NURBS-based Kirchhoff-Love shell analysis is briefly reviewed in Section 3. The new method based on the bending strips idea for general multi-patch shells is described in Section 4. In Section 5, the numerical results are presented, which include a set of well-known linear and non-linear benchmark problems. Application to a simplified model of a wind turbine blade, for which the wind loads were obtained from a separate fluid mechanics simulation, is also presented. In Section 6, the bending strip method is extended to successfully couple shells and solids. In Section 7, a study is performed to assess the behavior of the numerical solution for a range of the bending strip stiffness values. Recommendations are made on how to choose the bending strip stiffness parameter to ensure solution accuracy and reasonable condition number of the resultant stiffness matrix. In Section 8, we draw conclusions.

2. Kirchhoff-Love shell theory

In this section we present the governing equations of the Kirchhoff-Love shell theory. The theory is appropriate for thin shell structures and requires no rotational degrees of freedom. The variational formulation of a Kirchhoff-Love shell is based on the principle of virtual work expressed as

$$\delta W = \delta W_{int} + \delta W_{ext} = 0\,, \tag{1}$$

where W, W_{int}, and W_{ext} denote the total, internal, and external work, respectively, and δ denotes a variation with respect to the virtual displacement variables $\delta\mathbf{u}$, that is

$$\delta W = \frac{\partial W}{\partial \mathbf{u}}\delta\mathbf{u}\,. \tag{2}$$

The internal virtual work is defined by (see, e.g., [38])

$$\delta W_{int} = -\int_V (\mathbf{S} : \delta\mathbf{E})\, dV\,, \tag{3}$$

where V is the shell volume in the reference configuration (the total Lagrangian approach is adopted in this work), $\mathbf{E}$ is the Green-Lagrange strain tensor, $\delta\mathbf{E}$ is its variation with respect to virtual displacements $\delta\mathbf{u}$, and $\mathbf{S}$ is the energetically conjugate second Piola-Kirchhoff stress tensor.

For shell theory, the three-dimensional continuum description is reduced to that of the shell midsurface, and the transverse normal stress is neglected. Furthermore, the Kirchhoff-Love theory assumes that the shell cross sections remain normal to its middle surface in the deformed configuration, which implies that the transverse shear strains are zero. As a result, only in-plane stress and strain tensors are considered, and Greek indices, $\alpha = 1, 2$ and $\beta = 1, 2$, are employed to denote their components.

The components of the Green-Lagrange strain tensor are separated into two parts corresponding to membrane and bending action as follows:

$$E_{\alpha\beta} = \varepsilon_{\alpha\beta} + \theta^3 \kappa_{\alpha\beta} \,, \tag{4}$$

where $\theta^3 \in [-0.5t, 0.5t]$ is the through-thickness coordinate, t is the shell thickness, $\varepsilon_{\alpha\beta}$ are the membrane strains given by

$$\varepsilon_{\alpha\beta} = \frac{1}{2}(g_{\alpha\beta} - G_{\alpha\beta}) \,, \tag{5}$$

and $\kappa_{\alpha\beta}$ are the changes in curvature defined as

$$\kappa_{\alpha\beta} = b_{\alpha\beta} - B_{\alpha\beta} \,. \tag{6}$$

In (5), the covariant metric tensors are given by

$$g_{\alpha\beta} = \mathbf{g}_\alpha \cdot \mathbf{g}_\beta = \mathbf{x}_{,\alpha} \cdot \mathbf{x}_{,\beta} \,, \tag{7}$$

$$G_{\alpha\beta} = \mathbf{G}_\alpha \cdot \mathbf{G}_\beta = \mathbf{X}_{,\alpha} \cdot \mathbf{X}_{,\beta} \,, \tag{8}$$

and in (6), the curvature tensors are defined as

$$b_{\alpha\beta} = -\mathbf{g}_{\alpha,\beta} \cdot \mathbf{g}_3 \,, \tag{9}$$

$$B_{\alpha\beta} = -\mathbf{G}_{\alpha,\beta} \cdot \mathbf{G}_3 \,, \tag{10}$$

where $\mathbf{x}$ and $\mathbf{X}$ are the position vectors of material points in the current and reference configuration, respectively, and $(\cdot)_{,\alpha}$ denotes partial differentiation with respect to curvilinear coordinates θ_α, which in this case coincide with the NURBS parametric coordinates. In equations (9)-(10), $\mathbf{g}_3$ and $\mathbf{G}_3$ are the unit vectors in the direction normal to the shell midsurface in the current and reference configurations, respectively.

In equation (4), the components of the Green-Lagrange strain tensor are given with respect to the contravariant basis vectors $\mathbf{G}^\alpha$ that are related to the covariant basis vectors $\mathbf{G}_\beta$ as

$$\mathbf{G}^\alpha = [G_{\alpha\beta}]^{-1} \mathbf{G}_\beta \,. \tag{11}$$

Given the covariant basis, we define the local orthonormal basis $\bar{\mathbf{e}}_\alpha$ by orienting it on $\mathbf{G}_1$ as follows:

$$\bar{\mathbf{e}}_1 = \frac{\mathbf{G}_1}{\|\mathbf{G}_1\|} \,, \tag{12}$$

$$\bar{\mathbf{e}}_2 = \frac{\mathbf{G}_2 - (\mathbf{G}_2 \cdot \bar{\mathbf{e}}_1)\bar{\mathbf{e}}_1}{\|\mathbf{G}_2 - (\mathbf{G}_2 \cdot \bar{\mathbf{e}}_1)\bar{\mathbf{e}}_1\|} \,. \tag{13}$$

Remark: Equivalently, the local basis could be oriented on the second covariant basis vector. The choice of one or the other definition makes no difference in

the modeling of isotropic materials. However, for the orthotropic case, the two definitions must be distinguished.

Given the local basis in equations (12)-(13), we employ the following linear orthotropic stress-strain relationship in the local coordinate system

$$\begin{bmatrix} \bar{S}^{11} \\ \bar{S}^{22} \\ \bar{S}^{12} \end{bmatrix} = \overline{\mathbf{C}} \begin{bmatrix} \bar{E}_{11} \\ \bar{E}_{22} \\ 2\bar{E}_{12} \end{bmatrix}, \tag{14}$$

where

$$\overline{\mathbf{C}} = \begin{bmatrix} \dfrac{E_1}{(1-\nu_{12}\nu_{21})} & \dfrac{\nu_{21}E_1}{(1-\nu_{12}\nu_{21})} & 0 \\ \dfrac{\nu_{12}E_2}{(1-\nu_{12}\nu_{21})} & \dfrac{E_2}{(1-\nu_{12}\nu_{21})} & 0 \\ 0 & 0 & G_{12} \end{bmatrix}. \tag{15}$$

In equation (15), E_1 and E_2 are the Young's moduli in the directions defined by the local basis vectors, ν's are the Poisson ratios, G_{12} is the shear modulus, and $\nu_{21}E_1 = \nu_{12}E_2$ to ensure the symmetry of the constitutive material matrix $\overline{\mathbf{C}}$. In the case of an isotropic material, $E_1 = E_2 = E$, $\nu_{21} = \nu_{12} = \nu$, and $G_{12} = E/(2(1+\nu))$.

Introducing (14) and (4) into the expression for the internal virtual work given by equation (3), and pre-integrating through the shell thickness, we obtain

$$\delta W_{int} = -\int_A \left(t\, \overline{\boldsymbol{\varepsilon}}^T \overline{\mathbf{C}} \delta\overline{\boldsymbol{\varepsilon}} + \frac{t^3}{12}\, \overline{\boldsymbol{\kappa}}^T \overline{\mathbf{C}} \delta\overline{\boldsymbol{\kappa}} \right) dA\,, \tag{16}$$

where $\overline{\boldsymbol{\varepsilon}}$ and $\overline{\boldsymbol{\kappa}}$ are the vectors of membrane strain and curvature tensor coefficients in Voigt notation (in the local coordinate system), and dA is a differential area of the shell midsurface.

3. Analysis of one-patch and simple multi-patch NURBS shell structures

To obtain a conforming discretization of the Kirchhoff-Love variational shell theory, the underlying basis functions must be C^1-continuous. This is easily achieved using NURBS-based isgeometric analysis if a single patch geometry representation is employed. The multi-patch case is more complicated and requires additional treatment.

A NURBS surface for patch i, $\mathbf{S}^i(\theta_1, \theta_2) \in \mathbb{R}^d$, $d = 2, 3$, is defined parametrically as

$$\mathbf{S}^i(\theta_1, \theta_2) = \sum_{a=1}^{n_1} \sum_{b=1}^{n_2} \mathbf{P}^i_{a,b} R^i_{a,b}(\theta_1, \theta_2)\,, \tag{17}$$

where θ_1 and θ_2 are the parametric coordinates that coincide with the shell mid-surface convective coordinates, n_1 and n_2 are the number of univariate B-spline

functions in the two parametric directions, $\mathbf{P}$'s are the control points, and R's are the NURBS basis functions given by

$$R^i_{a,b}(\theta_1,\theta_2) = \frac{w^i_{a,b} N^i_a(\theta_1) N^i_b(\theta_2)}{\sum_{c=1}^{n_1}\sum_{d=1}^{n_2} w^i_{c,d} N^i_c(\theta_1) N^i_d(\theta_2)}\,. \tag{18}$$

In equation (18), w's are non-negative scalar weights and N's are the univariate B-spline basis functions (see, e.g., [39, 40]).

The parametric space is sub-divided into elements by knots. NURBS basis functions are C^∞-continuous on the element interiors and C^{p-k}-continuous at the element boundaries, where p is the polynomial order and k is the knot multiplicity of the univariate B-splines. As a result, quadratic or higher-order NURBS are necessary for Kirchhoff-Love shell analysis. Note that, if two different polynomial orders are employed in two parametric directions, the continuity of the basis is also different in these directions.

The Kirchhoff-Love shell equations are discretized using Galerkin's method. The shell displacements for patch i are expanded in terms of the same NURBS basis functions used for the definition of the shell midsurface geometry, namely

$$\mathbf{u}^i(\theta_1,\theta_2) = \sum_{a=1}^{n_1}\sum_{b=1}^{n_2} \mathbf{u}^i_{a,b} R^i_{a,b}(\theta_1,\theta_2)\,, \tag{19}$$

where $\mathbf{u}^i_{a,b}$'s are the displacement control variables.

Kirchhoff-Love shell analysis of structures composed of multiple NURBS patches requires additional treatment. An approach was presented in [1] that is based on enforcing linear constraints between displacement control variables at the adjacent NURBS patches to maintain a conforming discretization. The approach and its inherent limitations are reviewed in what follows.

For the connection of two patches, two basic cases need to be distinguished.

G^1-continuous connection. For parametric surfaces, G^1-continuity means that two surfaces joining at a common edge have a common tangent plane at each point along that edge. For NURBS surfaces this condition is satisfied if the control points across the common edge are colinear, that is,

$$\mathbf{P}^2_{2,j} = (1+c)\,\mathbf{P}^1_{n,j} - c\,\mathbf{P}^1_{n-1,j}\,, \tag{20}$$

where c is a scalar. For rotation-free shell analysis, the above condition has to be maintained in the deformed state of the structure. For this, we impose the same co-linearity condition on the displacement control variables and their variations, namely,

$$\mathbf{u}^2_{2,j} = (1+c)\,\mathbf{u}^1_{n,j} - c\,\mathbf{u}^1_{n-1,j}\,, \tag{21}$$

$$\delta \mathbf{u}^2_{2,j} = (1 + c)\, \delta \mathbf{u}^1_{n,j} - c\, \delta \mathbf{u}^1_{n-1,j}\,. \tag{22}$$

Equations (21)-(22) represent a linear constraint that can be fulfilled exactly at the analysis level. Although the approach leads to the desired results, explicitly writing down the above constraints for every control point at the patch interface seems like a cumbersome task that is inefficient for a large number of patches.

Connection with a kink. If two parametric surfaces are joined with a kink (i.e., a C^0 connection with no common tangent plane), the angle between the patches has to be maintained in the deformed configuration. Similar to the G^1-continuous case, this may be achieved by coupling the respective control points along a common edge. For each triple of control points $\mathbf{P}^2_{2,j}, \mathbf{P}^1_{n,j}$ and $\mathbf{P}^1_{n-1,j}$, the angle spanned by these control points must remain constant during deformation. The angle may be expressed using the scalar product formula

$$\alpha = \cos^{-1}\left(\frac{\left(\mathbf{P}^1_{n,j} - \mathbf{P}^1_{n-1,j}\right) \cdot \left(\mathbf{P}^2_{2,j} - \mathbf{P}^1_{n,j}\right)}{\left|\mathbf{P}^1_{n,j} - \mathbf{P}^1_{n-1,j}\right| \cdot \left|\mathbf{P}^2_{2,j} - \mathbf{P}^1_{n,j}\right|} \right), \tag{23}$$

which does not lead to a linear constraint relationship for the displacement degrees of freedom in the general case. As a result, the angle constraint cannot be enforced in a strong sense by a direct coupling of degrees of freedom as in the G^1-continuous case.

In the sequel, we propose a method that circumvents the difficulties in the previously proposed approaches to handle multi-patch shell geometries. The idea is to maintain the above mentioned constraints between the displacement degrees of freedom in an approximate sense, rather than strongly. The method makes no distinction between the two situations presented above and applies to a general class of multi-patch shell structures.

4. The bending strip method

The method we propose to handle complex multi-patch shell structures consists of modeling structural geometry using NURBS patches that are joined with C^0-continuity. In addition, strips of fictitious material modeled as surface NURBS patches are placed at patch intersections. The schematic of the proposed approach is illustrated in Figure 1 for a two-patch case. The triples of control points at the patch interface, consisting of a shared control point and one on each side, are extracted and used as a control net for the bending strip. The parametric domain of the bending strip consists of one quadratic element in the direction transverse to the strip and, for simplicity and computational efficiency, of as many linear elements as necessary to accommodate all the control points along the length of the strip. The material is assumed to have zero mass (for dynamic simulations, not considered in

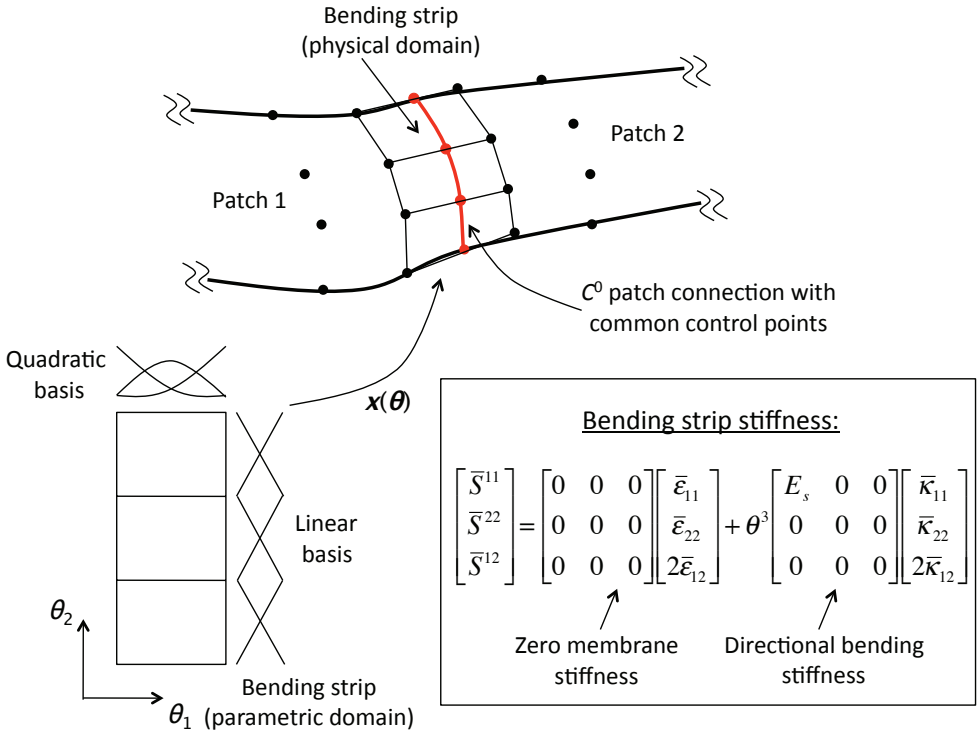

Figure 1: Schematic of the bending strip method.

this paper), zero membrane stiffness and non-zero bending stiffness only in the direction transverse to the strip. The transverse direction is obtained using the local basis construction in Section 2. Mathematically, the method consists of augmenting the principle of virtual work with additional terms of the form

$$\delta W_{int}^{s} = -\int_{A} \frac{t^3}{12} \, \overline{\boldsymbol{\kappa}}^{T} \overline{\mathbf{C}}_{s} \delta \overline{\boldsymbol{\kappa}} \, dA \tag{24}$$

for every bending strip. The bending strip constitutive material matrix $\overline{\mathbf{C}}_s$ is given by

$$\overline{\mathbf{C}}_{s} = \begin{bmatrix} E_s & 0 & 0 \\ 0 & 0 & 0 \\ 0 & 0 & 0 \end{bmatrix}, \tag{25}$$

where E_s is the directional bending stiffness. This design of the material constitutive matrix ensures that the bending strips add no extra stiffness to the structure. They only penalize the change in the angle during the deformation between the triples of control points at the patch interface. The stiffness E_s must be high enough that the change in angle is within an acceptable tolerance. However, if E_s is chosen too high, the global stiffness matrix becomes badly conditioned, which may lead to divergence in the computations. In the numerical examples section of this paper,

the effect of different bending stiffnesses is investigated to find a range of values, which can be used in the general case.

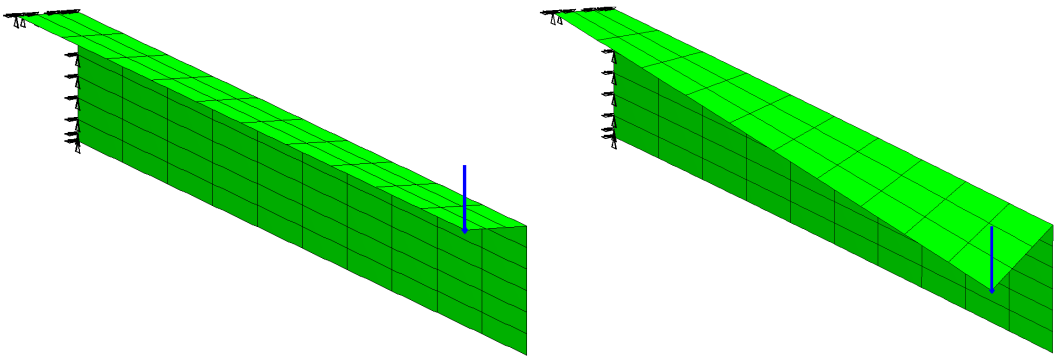

(a) (b)

Figure 2: L-shaped cantilever with a point load. (a) Two rectangular patches meeting at a 90° angle. (b) Deformed configuration with no bending strip. The connection acts like a hinge.

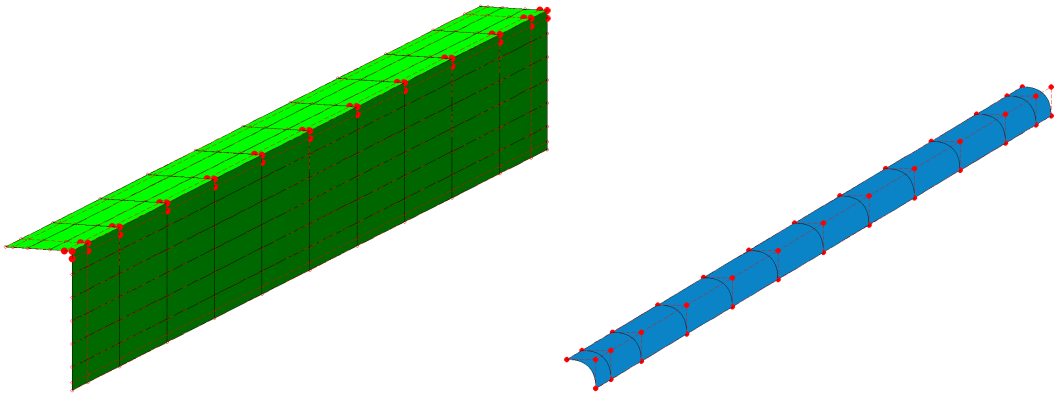

(a) (b)

Figure 3: L-shaped cantilever with a point load. (a) Structure with control points coupled to a bending strip highlighted. (b) Bending strip corresponding to an L-shaped configuration.

The method is illustrated by the example of an L-shape cantilever with a point load. Figure 2a shows the geometry consisting of two rectangular patches meeting at a 90° angle, which corresponds to the connection with a kink. Figure 2b shows the deformed configuration for the case when the patches are connected with C^0-continuity only, i.e., without the bending strip. As can be seen, the C^0-continuous connection unintentionally acts like a hinge between the patches, and no bending moment is transferred. The situation is rectified by adding a bending strip. In Figure 3a, the control points to be coupled by the bending strip are highlighted, while Figure 3b shows the bending strip built using these control points. In Figure 4, the resulting deformation with the bending strip is shown. As can be seen, the angle between the patches remains nearly constant during deformation.

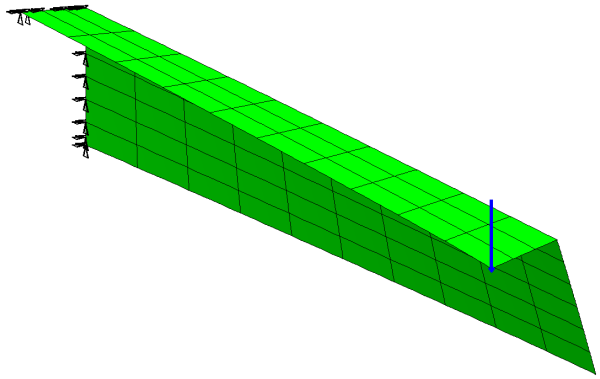

Figure 4: L-shaped cantilever with a point load. Deformed configuration with a bending strip. Angle between the patches remains nearly constant throughout the deformation.

5. Numerical Examples

5.1. Shell obstacle course

The first examples are taken from the well-known shell obstacle course proposed by Belytschko et al. [41]. It consists of three problems, namely the Scordelis-Lo roof, the hemispherical shell and the pinched cylinder. All three problems are modeled using multi-patch shells with bending strips and the results are compared with single patch solutions. Linearized theory is employed in these examples.

5.1.1. Scordelis-Lo roof

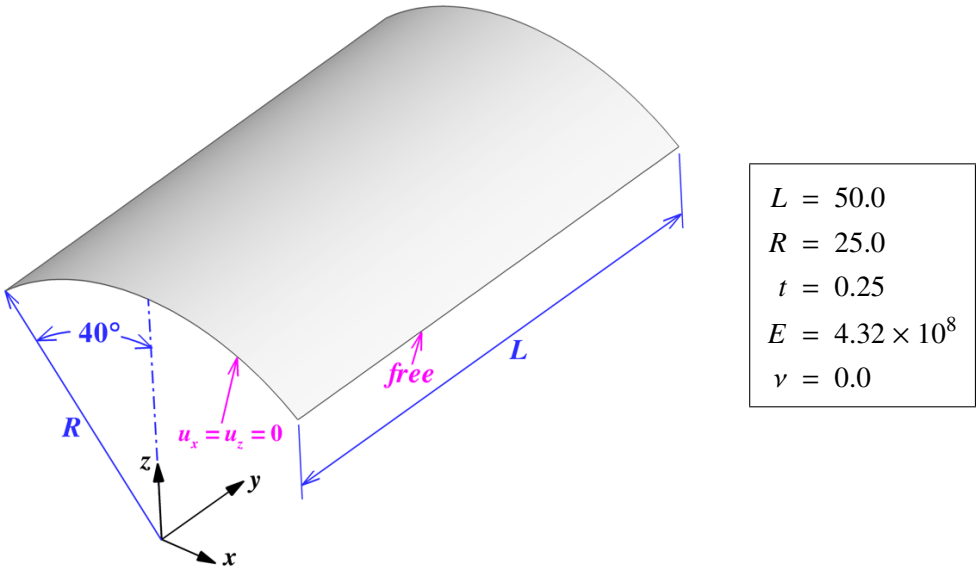

Figure 5: Scordelis-Lo roof. Problem description. The roof is subjected to a uniform vertical gravity load of 90.0 per unit area. The ends are supported by rigid diaphragms.

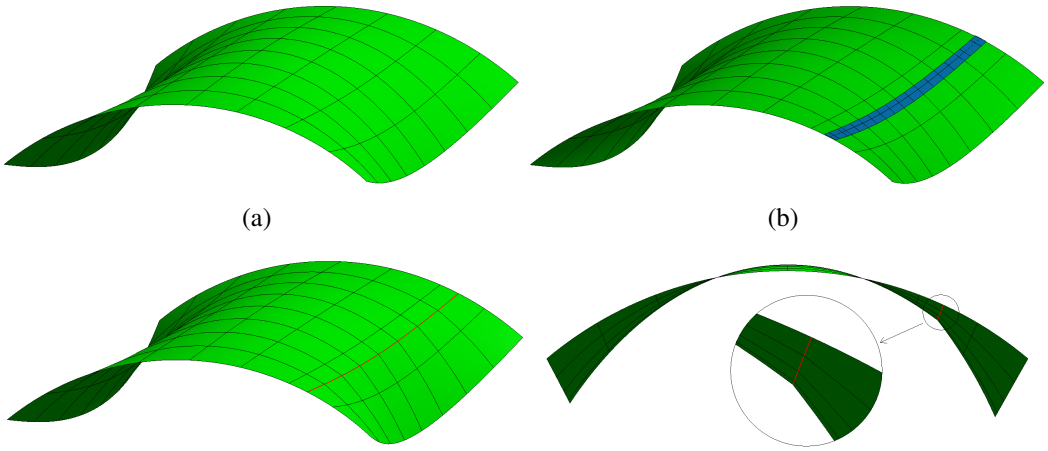

(a) (b)

(c)

Figure 6: Scordelis-Lo roof. (a) Deformed configuration for a single patch computation (scaling factor of 10 is applied to the displacement). (b) Deformed configuration for a two-patch computation with a bending strip. The resulting deformation is nearly identical to the single-patch conforming solution. (c) Deformed configuration for a two-patch computation and no bending strip. A kink in the deformed geometry is clearly visible.

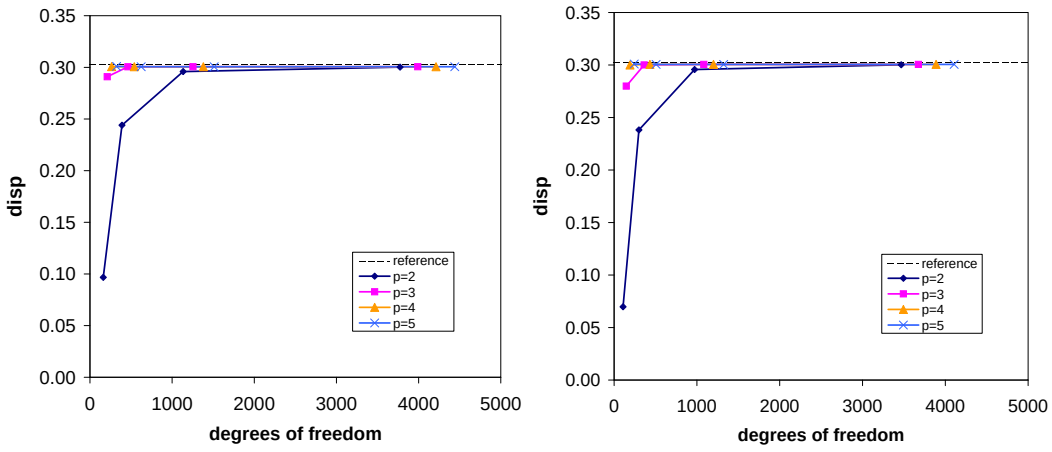

(a) (b)

Figure 7: Scordelis-Lo roof. k-refinement study. (a) Two-patch computation with a bending strip. (b) Single patch computation. Convergence behavior is nearly identical in both cases.

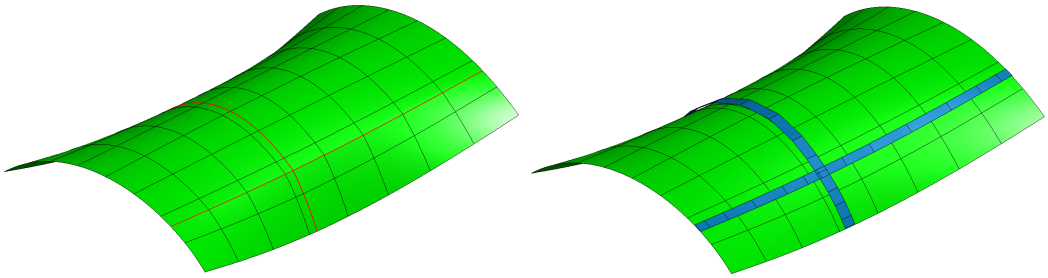

(a) (b)

Figure 8: Scordelis-Lo roof. (a) Decomposition of the problem domain into four patches. (b) Two overlapping bending strips used in the computation.

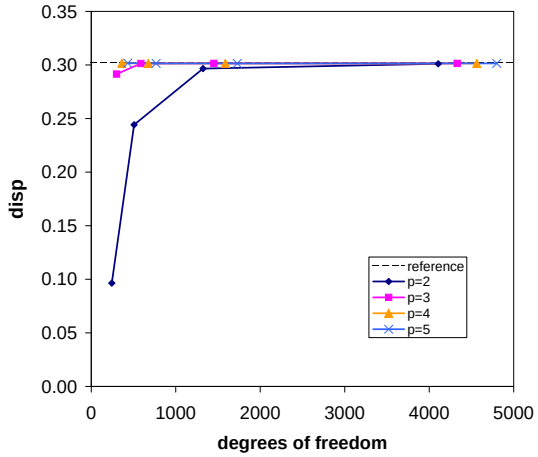

Figure 9: Scordelis-Lo roof. *k*-refinement study with two overlapping bending strips.

This problem consists of a section of a cylindrical shell subjected to a uniform gravity load, and supported by rigid diaphragms at its ends, whereas the side edges are free (see Figure 5 for the problem geometry and material parameters, and Figure 6a for a single patch computation). The vertical displacement at the midpoint of the side edge is taken as a reference solution.

A line of C^0-continuity is created by repeated knot insertion. Figure 6c shows the roof with the C^0-continuity marked by a red line. A kink in the deformation can clearly be seen. The displacement for this non-conforming discretization converges to $u_z = -0.3871$, which significantly overestimates the reference value of $u_z = -0.3024$.

A bending strip with $E_s = E \times 10^3$ is added along the C^0-continuity line (see Figure 6d), and a k-refinement study of the roof with the strip is performed. Figure 7 shows convergence of the vertical displacement. Convergence results are compared with a single conforming patch (i.e., no C^0 lines). Similar convergence behavior is observed for both cases, indicating that the analysis results are not sensitive to the presence of the bending strip.

Remark: It should be noted that the bending strip is re-created for every new mesh in the refinement sequence according to its design. The cost of creating the new strips is negligible in comparison with the costs associated with mesh refinement. Due to the rectangular topology of NURBS patches, the bending strip control points may be easily extracted from the adjoining patches. It should also be noted that the polynomial order of the strip is fixed at quadratic in the transverse and linear in the longitudinal directions, independent of the polynomial order of the structural model. Finally, the width of the bending strip tends to zero as the mesh is h-refined.

To further test the method, a second line of C^0-continuity, orthogonal to the first one, is inserted and a second bending strip is introduced (see Figure 8). As can be seen from Figure 8b, the two strips overlap with each other. The results of the same convergence study are plotted in Figure 9. Similar convergence behavior is obtained as in the previous two cases, indicating that the bending strips are behaving according to their design.

Remark: An important feature of the proposed approach is that no interaction between the overlapping strips is introduced, making the method practical for large structures where more than two patches may meet at a point.

5.1.2. Hemispherical shell

A hemispherical shell is subjected to two diametrically opposite point loads. Figure 10 shows the problem setup. The bottom circumferential edge of the hemisphere is free. The reference solution is given as the radial displacement under the point loads and is equal to 0.0924. The hemisphere is modeled by four patches

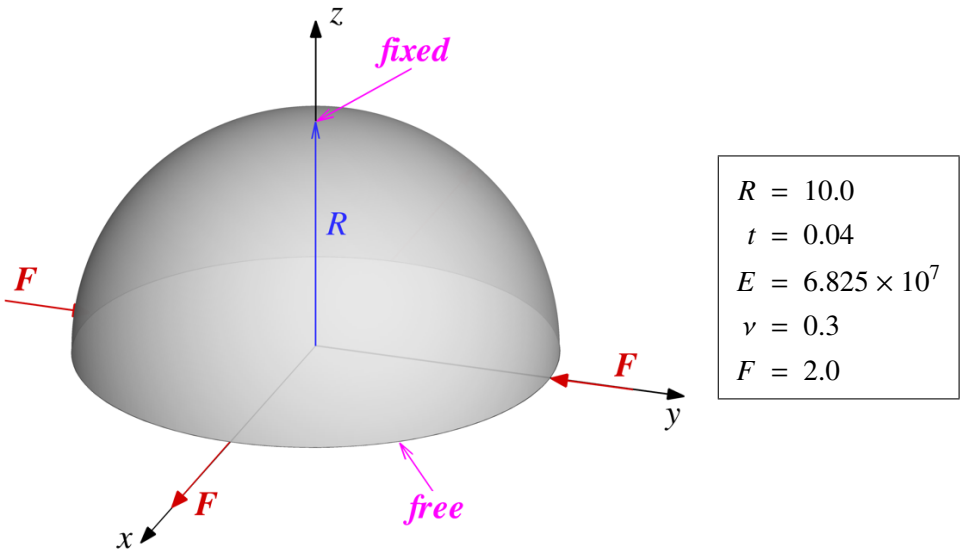

Figure 10: Hemispherical shell. Problem description. The hemisphere is subjected to two diametrically opposite point loads. The bottom circumferential edge is free.

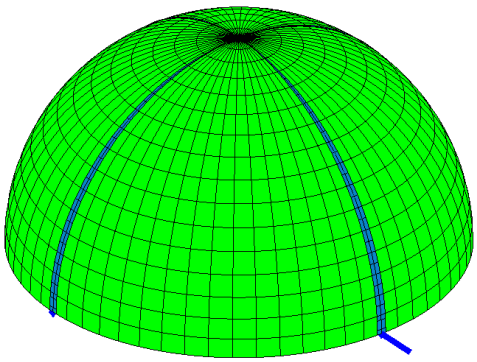

Figure 11: Hemispherical shell. The complete hemisphere is modeled by four patches with bending strips.

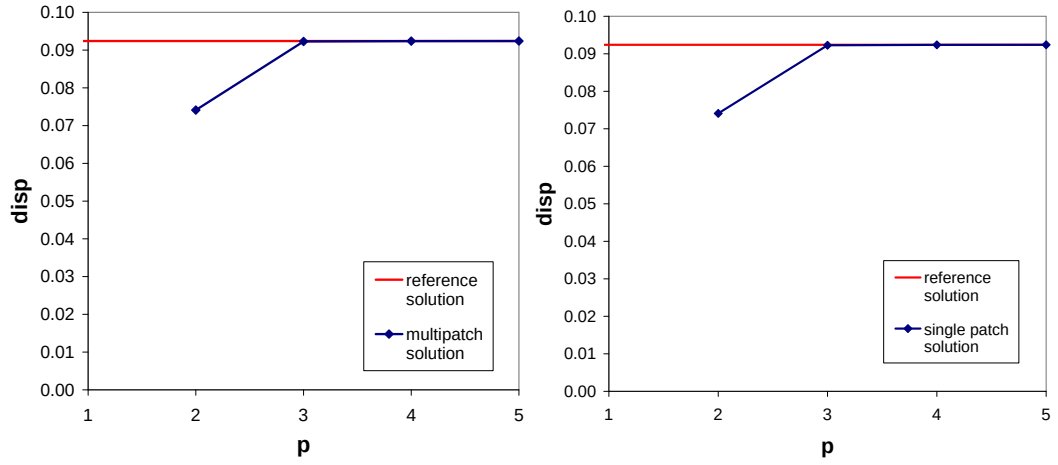

(a) (b)

Figure 12: Hemispherical shell. Displacement convergence under p-refinement. (a) Multi-patch computations with bending strips. (b) Single patch computation with symmetry boundary conditions. Convergence behavior is nearly identical in both cases.

which are connected by bending strips with $E_s = E \times 10^3$ (see Figure 11). A p-refinement study is performed where each patch is discretized using 16×16 elements, and polynomial degrees from quadratic to quintic are employed. The results are shown in Figure 12a. For comparison, the same refinement was performed on a quarter of the domain with symmetry boundary conditions for a single patch solution (see Figure 12b). Nearly identical results are obtained in both cases. The bending strips are performing as expected even in the presence of mesh degeneration at the top of the hemisphere.

5.1.3. Pinched Cylinder

In this example, a cylinder supported by rigid diaphragms at both ends is subjected to two diametrically opposite point loads as shown in Figure 13. Due to the problem symmetry only one half of the cylinder is modeled. The geometry consists of four patches which are connected by two bending strips with $E_s = E \times 10^3$ (see Figure 14). A $k-$refinement study is performed (Figure 15a) and the convergence results are compared to a single patch solution (Figure 15b) where only one-eighth of the cylinder with the respective symmetry conditions is computed. Nearly identical results are obtained in both cases.

5.2. Structures with large deformations

In this section we apply the developed method to two large-deformation benchmark problems. Both examples involve a cantilever plate under constant moment loading. In the first case the plate is bent into a circle and in the second case the plate is twisted.

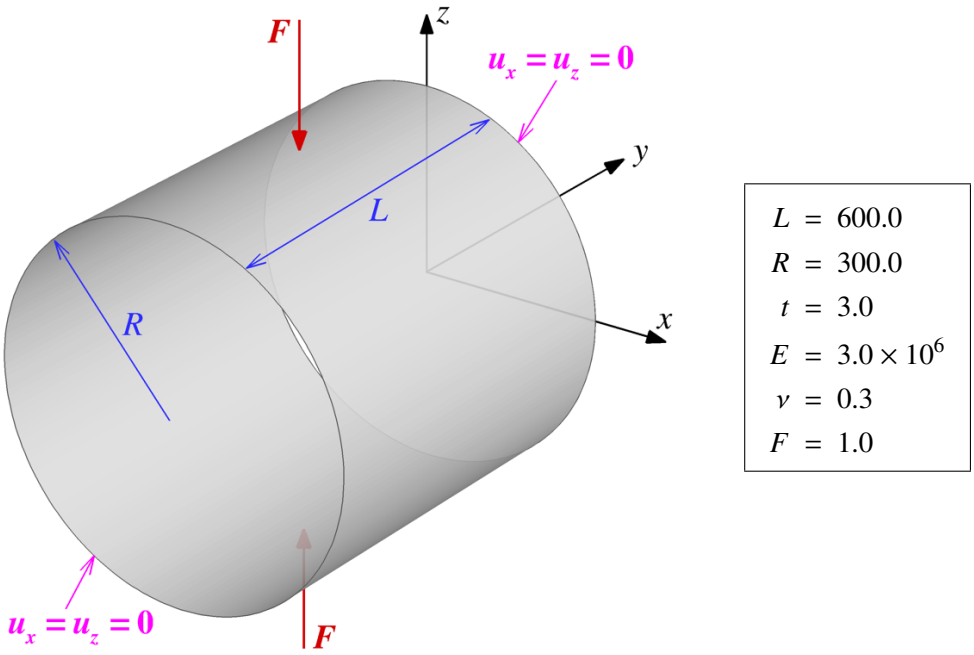

Figure 13: Pinched cylinder. Problem description. The cylinder is subjected to equal and opposite concentrated forces at its midspan. The ends are constrained by rigid diaphragms.

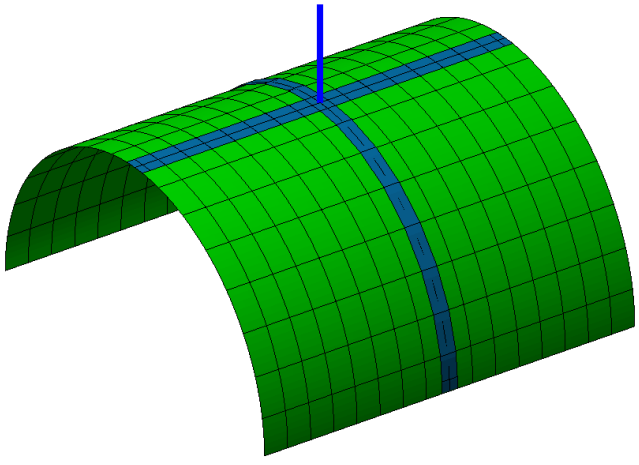

Figure 14: Pinched cylinder. Half of the cylinder is modeled by four patches with bending strips.

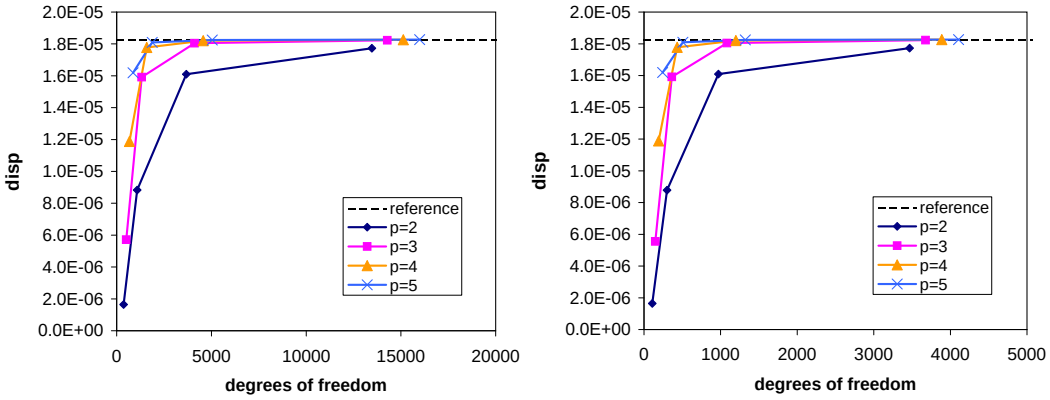

Figure 15: Pinched cylinder. *k*-refinement study. (a) Multi-patch computations with bending strips. (b) Single patch computation with symmetry boundary conditions. Convergence behavior is nearly identical in both cases.

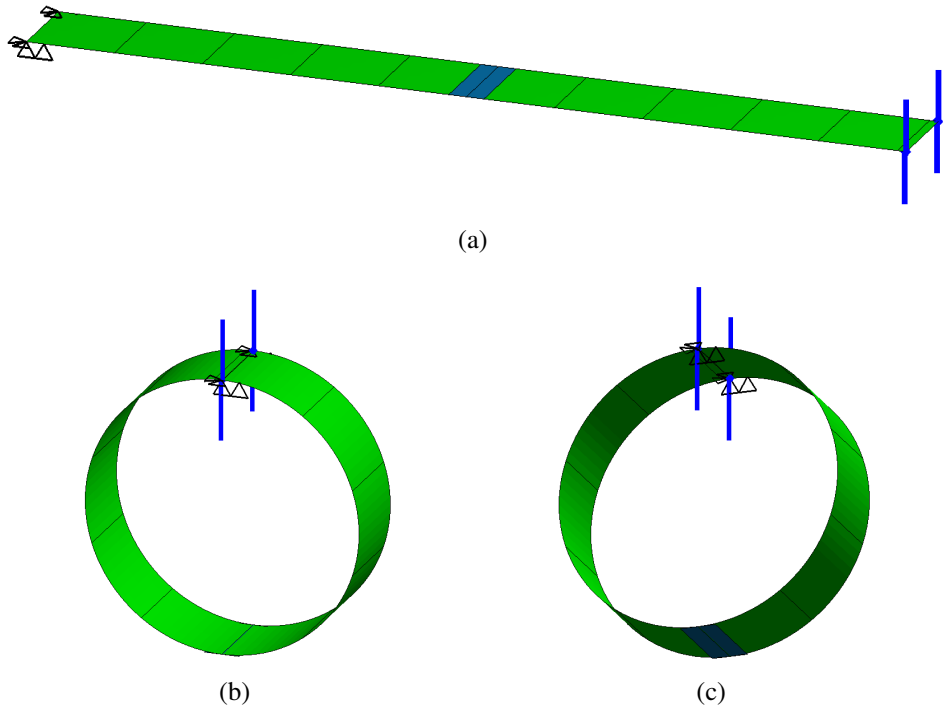

Figure 16: Bent plate. (a) Initial configuration. The bending moment is represented by two pairs of follower forces acting in opposite directions. (b) Deformed configuration. (c) Deformed configuration with a bending strip shown on the bottom.

5.2.1. Bent plate

The cantilever plate example is used to test the formulation in the large deformation regime. The problem setup is illustrated in Figure 16a. An external moment $M = \frac{2\pi EI}{L}$, where I and L are the plate moment of inertia and length, respectively, is applied at the tip. The expected plate deformation is such that the final configuration is a circle. The moment is modeled by two pairs of forces in opposite directions which follow the deformation. The plate is discretized by ten quintic NURBS elements of full continuity and the strip stiffness is chosen as $E_s = E \times 10^3$. A C^0 line is introduced in the interior of the plate and the bending strip is added to the structure. Figures 16b and 16c show that the bending strip method also works well for very large deformations, as the cantilever plate deforms into a circle.

5.2.2. Twisted plate

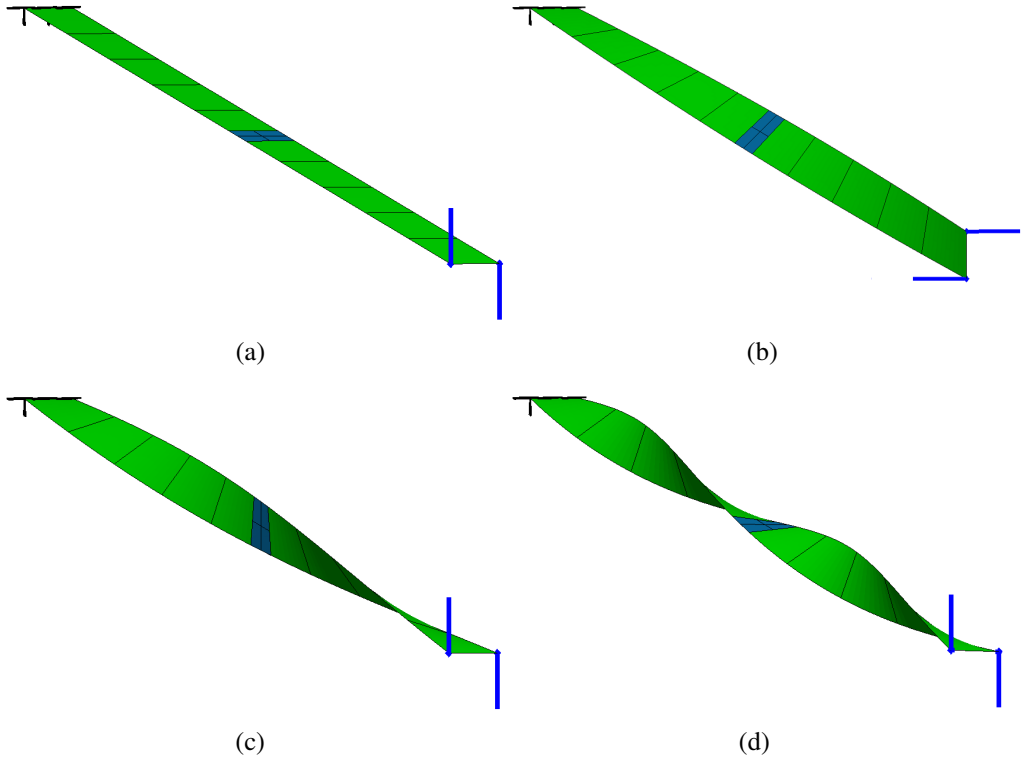

Figure 17: Twisted plate. (a) Initial configuration. The twisting moment is represented by a pair of follower forces acting in opposite directions. (b) Twisted by 90°. (c) Twisted by 180°. (d) Twisted by 360°.

Here the plate from the previous example is subjected to a pure twisting moment, which is also represented by a pair of follower forces with opposite directions. Quadratic basis functions are used in the width direction so that straight cross-sections, which are to be the expected, are not defined *ab initio*. Quintic NURBS are employed in the long direction. The results are compared to the refer-

ence results from the beam theory, i.e. $M_t = \theta \frac{GI_t}{L}$, where M_t is the torsional moment, θ is the twist angle at the tip, G is the shear modulus, I_t is the torsion constant, and L is the plate length. Using the above relationship, we apply the moment at the tip of the plate and compare the resultant twist angle to the expected one. We computed three cases corresponding to 90°, 180°, and 360° rotations. The results are collected in Figure 17 and the correct deformations are obtained in all cases. Also, in the deformed configuration, the plate cross-sections remain straight, which is consistent with the beam theory.

5.3. Application to a wind turbine rotor

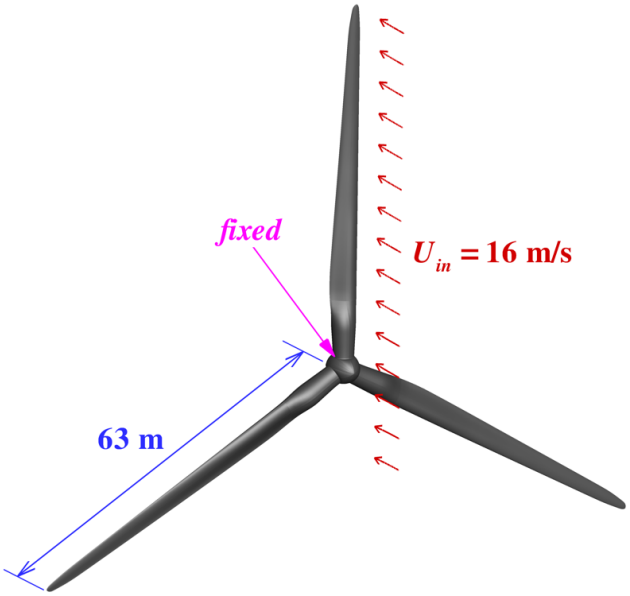

Figure 18: Wind turbine rotor. Problem description.

The problem setup and boundary conditions are shown in Figure 18. The geometry of the wind turbine rotor, based on the data reported in [42], is modeled using quadratic NURBS. A unidirectional E-glass/epoxy composite is used for the rotor blade material, and the corresponding orthotropic elastic moduli are given in Table 1. Only one rotor blade is considered in the analysis and its shell thickness distribution is presented in Figure 19a. A 16-patch NURBS model of the blade with bending strips is shown in Figure 19b. The blade is subjected to a wind load corresponding to 16 m/s wind obtained from a separate fluid mechanics simulation [43]. The blade deflects under the action of the wind and the deflection result is presented in Figure 19c. Maximum displacement occurs at the tip of the blade and equals to 2.96 m, which is a realistic value for this design and wind load levels.

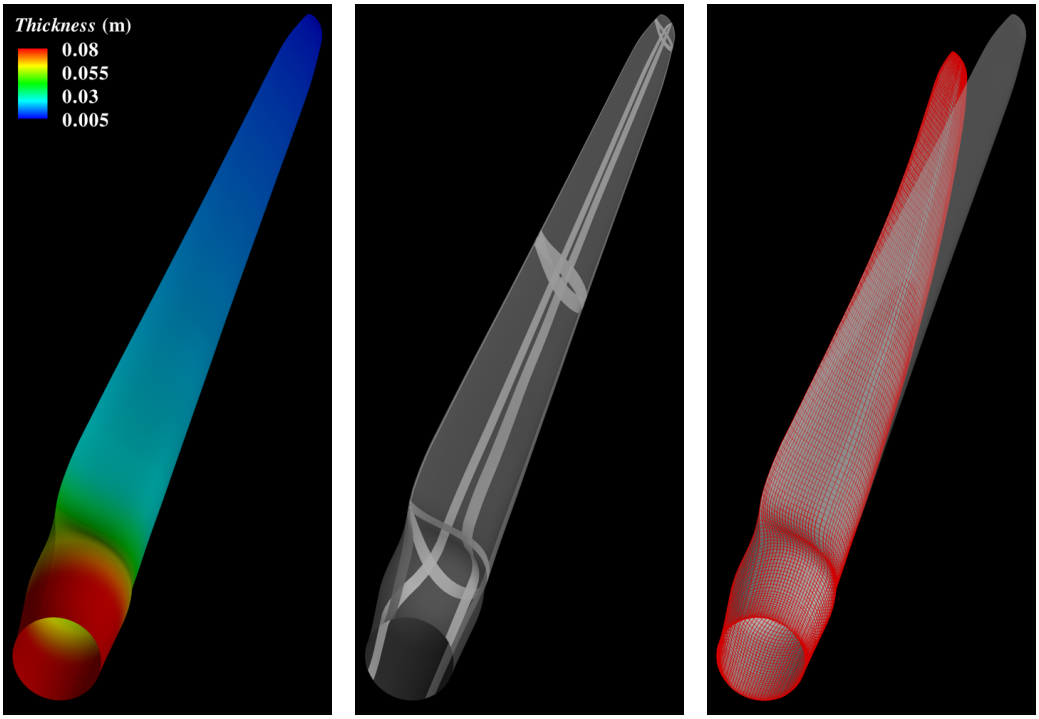

(a) (b) (c)

Figure 19: A single wind turbine rotor blade. (a) Shell thickness distribution. (b) A 16-patch NURBS model with bending strips. (c) Reference and deformed configurations.

E_1 (GPa)	E_2 (GPa)	G_{12} (GPa)	ν_{12}
39	8.6	3.8	0.28

Table 1: Material properties of a unidirectional E-glass/epoxy composite [44].

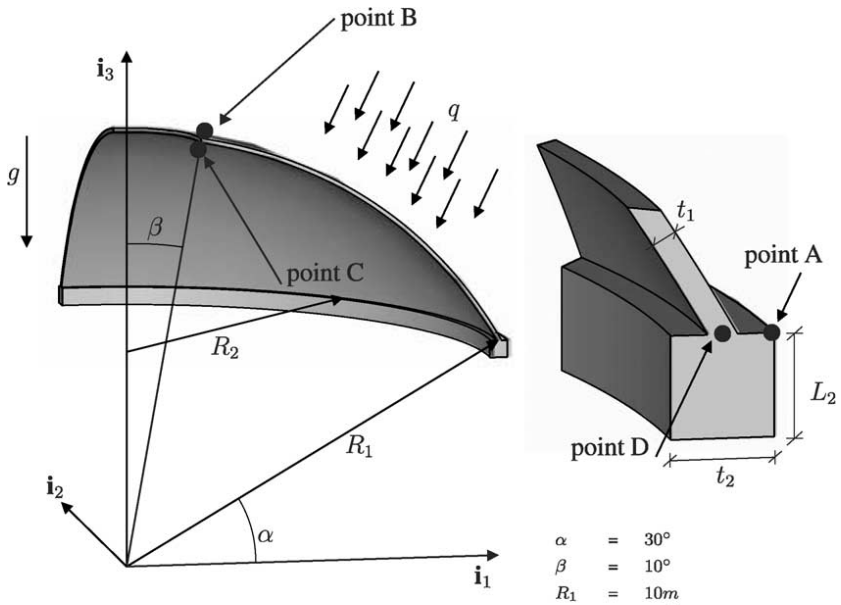

Symmetry to $\mathbf{i}_1$-$\mathbf{i}_3$-plane:
$\overset{k}{u}_2 = 0$ for $k = 0, \ldots, nk$

Symmetry to $\mathbf{i}_2$-$\mathbf{i}_3$-plane:
$\overset{k}{u}_1 = 0$ for $k = 0, \ldots, nk$

Boundary conditions:
$\overset{k}{u}_3 = 0$ for $k = 0, \ldots, nk$

α	=	$30°$
β	=	$10°$
R_1	=	$10m$
R_2	=	$5\sqrt{3}m$
t_1	=	$0.1m$
t_2	=	$0.4m$
L_2	=	$0.4m$
E	=	$6.825 \cdot 10^7 \frac{kN}{m^2}$
ν	=	0.3
ρ	=	$500 \frac{kg}{m^3}$
g	=	$10.0 \frac{m}{s^2}$
q	=	$100.0 \frac{kN}{m^2}$

Figure 20: Hemispherical shell with a stiffener. Problem setup from [45]

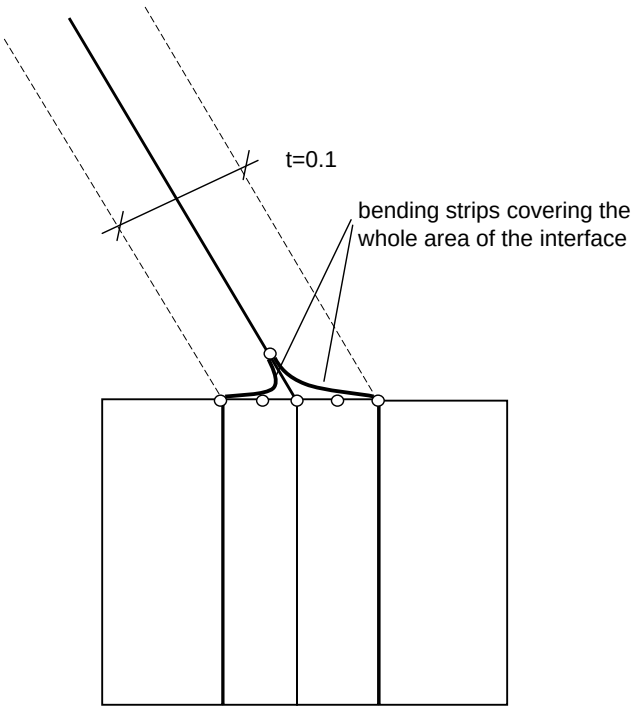

Figure 21: Hemispherical shell with a stiffener. Solid-shell coupling using bending strips.

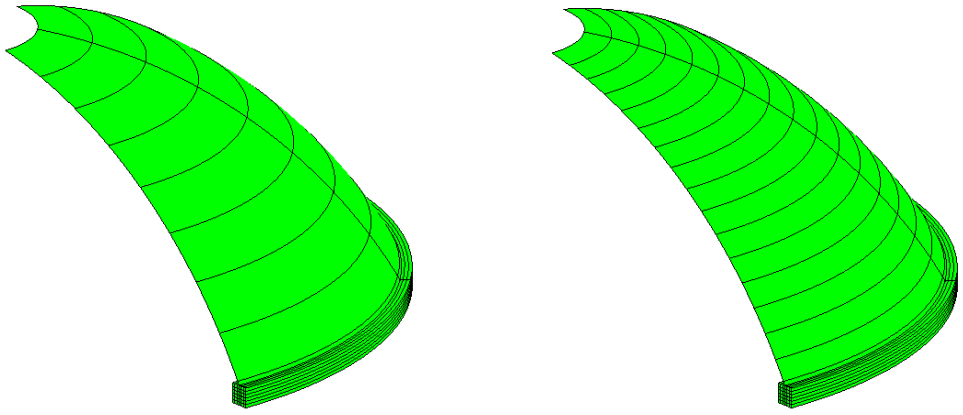

(a) Mesh 1 (b) Mesh 2

Figure 22: Hemispherical shell with a stiffener. Meshes employed for a $p-$refinement study.

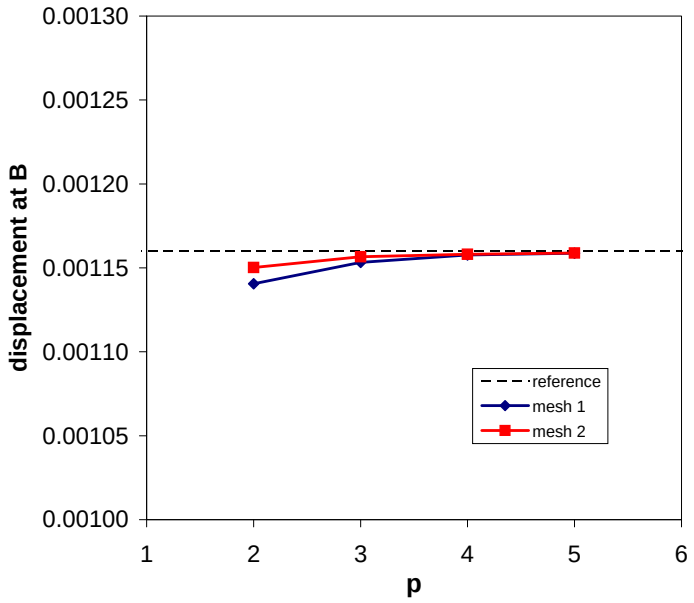

Figure 23: Hemispherical shell with a stiffener. Displacement convergence at point B.

6. Bending strip method for coupling of shells and solids

The need for coupling of shells and solids arises in many structural mechanics applications. This situation presents a computational challenge, because a) a shell often makes use of rotational degrees of freedom, which cannot be directly transfered to the solid, and b) a shell is modeled by its midsurface, which is a set of measure zero that may introduce singularities in the solid, and requires special treatment. In this section, we propose to extend the bending strip approach for the coupling of rotation-free shells and solids. The method consists of connecting a solid and a shell along a line in a C^0-compatible fashion, and adding bending strips that cover the area of the their intersection. This necessitates the use of bending strips with more than one quadratic element in the transverse direction and as many control points as the solid has in the overlap region. As a result, the strip does not disappear under mesh refinement and its width stays finite and equal to that of the overlap region.

We use the "hemispherical shell with a stiffener" problem presented in Rank et al. [45] to illustrate our approach. The problem setup is depicted in Figure 20. Rank et al. have used two different methods to solve this problem: a) a hierarchical shell approach where both shell and stiffener are modeled with high-order shell elements and b) a 3D solid formulation for both shell and stiffener based on $p-$version hexahedral finite elements. Here we use a hybrid approach, in which we model the stiffener as a 3D solid and the hemisphere as a Kirchhoff-Love shell. Four solid patches are used to model the stiffener. They are connected with C^0-continuity in places that correspond to the shell midsurface and its two outer surfaces. Figure 21 illustrates the shell-solid intersection and the bending strips. The dashed lines show

the real 3D dimensions of the shell while its midsurface is depicted by a solid line. The bending strips, placed on both sides of the shell, cover the entire overlap region.

A $p-$refinement study was performed using two different NURBS meshes. The results for the displacement at point B, located at the tip of the shell, are compared to those of [45]. Figure 22 shows the meshes. In both cases, two cubic elements are used in the circumferential direction. The stiffener cross section is discretized using 6×6 rectangular elements. Mesh 1 and Mesh 2 use 8 and 16 elements, respectively, in the meridian direction (see Figure 22). In the $p-$refinement study, the polynomial degree was raised from quadratic to quintic for both the shell and stiffener. No refinement was necessary in the circumferential direction due to axisymmetry. The displacement at point B is plotted in Figure 23. Rapid convergence to the reference value is observed for both discretizations.

7. Choosing a reliable bending strip stiffness

Here we revisit several numerical examples from the previous section and examine the behavior of the solution for a wide range of the bending stiffness values. This is done in an effort to gain initial understanding of its effect on the solution as well as to give a recommendation as to what values to chose in practical computations.

7.1. Cantilever plate

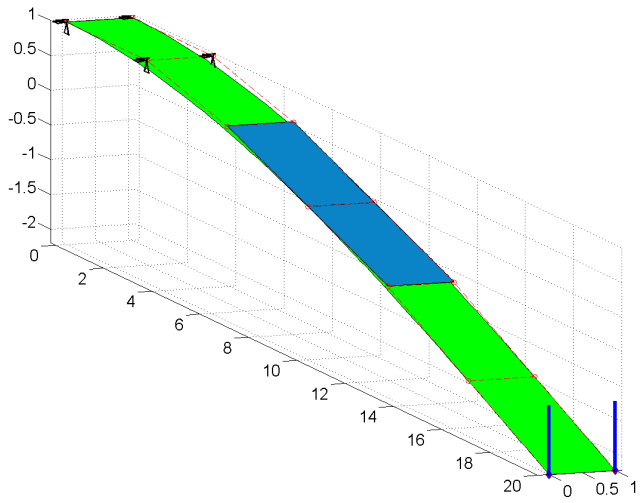

Figure 24: A two-patch model of a cantilever plate connected with a bending strip in a displaced configuration.

We again consider a simple cantilever plate, which is cut into two patches at the middle of its length (see Figure 24). The displacement at the tip of the cantilever is computed for different values of E_s, and is compared to the reference solution from the linear beam theory. The results are collected in Figure 25. For all ratios $E_s/E \geq 10^3$ the relative error is less than 10^{-3}. We would like to note that despite a

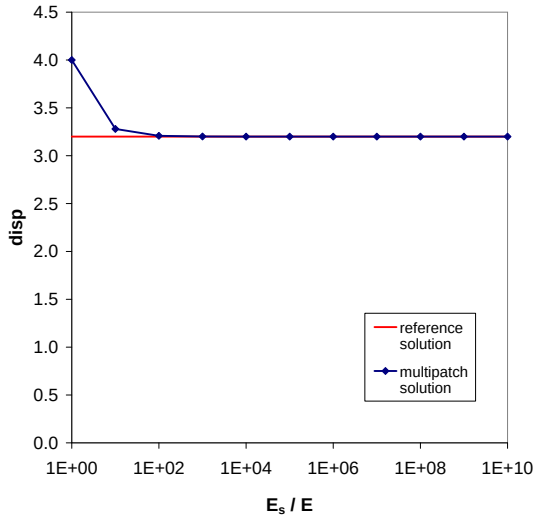

Figure 25: Cantilever plate tip displacement as a function of the bending strip stiffness.

considerable overlap between the bending strip and the two patches, no additional stiffness of the structure is introduced. The strip merely enforces G^1-continuity at the patch interface.

7.2. L-shaped cantilever

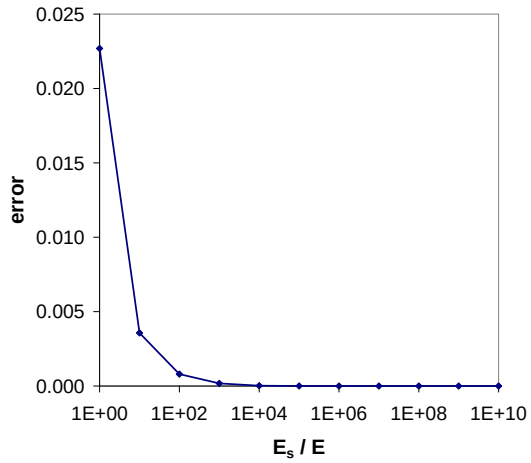

Figure 26: L-shape cantilever. Relative change in the angle between two patched at the cantilever tip as a function of the bending strip stiffness.

In the following study, the cantilever shown in Figure 2a is computed for different stiffness values of the strip, and the change in the angle between the two patches at the tip is recorded. The strip stiffness E_s is chosen as $E_s = E \times 10^{\alpha}$, and the computations were performed for $\alpha = 0, ..., 10$. The results are collected in Figure 26. The change in the angle decreases with increasing α, as expected. For stiffness ratio $E_s/E = 10^3$, the relative error is less than 10^{-3}. Further computations reveal that

the solution becomes unstable for strip stiffness ratio $E_s/E > 10^{13}$. This suggests that there is a relatively large range of α for which the bending strip method yields correct and stable solutions.

7.3. V-shaped arch

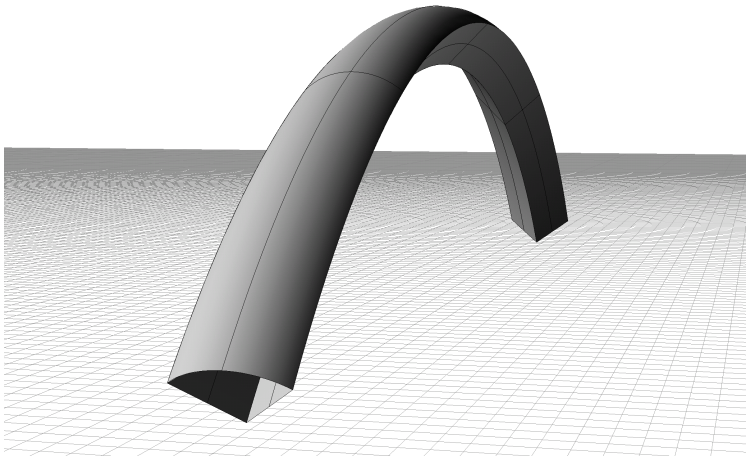

Figure 27: A three-patch model of a V-shaped arch created in Rhino [46] and exported to the isogeometric shell analysis software via an user-implemented plugin.

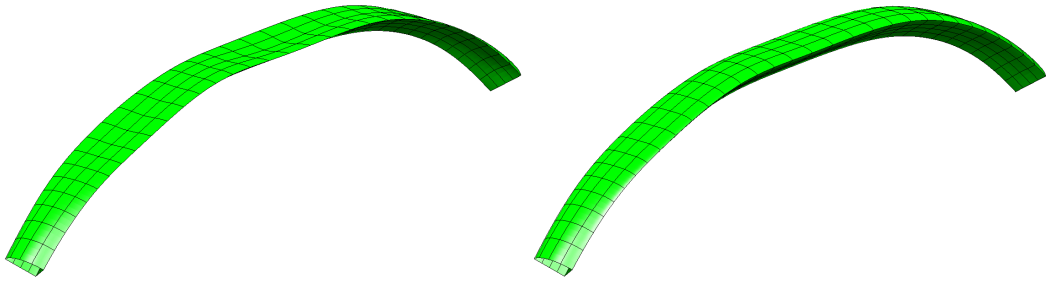

(a) (b)

Figure 28: V-shaped arch. Deformed configuration due to a constant load applied to the top patch. (a) Results without bending strips. (b) Results with bending strips.

This example is a geometrically more complex problem than the L-shaped cantilever described above. The geometry, created in a NURBS-based CAD program Rhino [46], consists of three NURBS patches and is shown in Figure 27. The arch is fixed at its ends and subjected to a constant load applied to the top patch. A user-implemented Rhino plugin [47] is employed to set up the model and export it to the isogeometric analysis software. The geometry is further refined in the analysis code, and the resulting deformations with and without bending strips are shown in Figure 28. Note that in the case of no bending strips the deformation is non-physical in that the C^0 line produces unintended "hinge" effect.

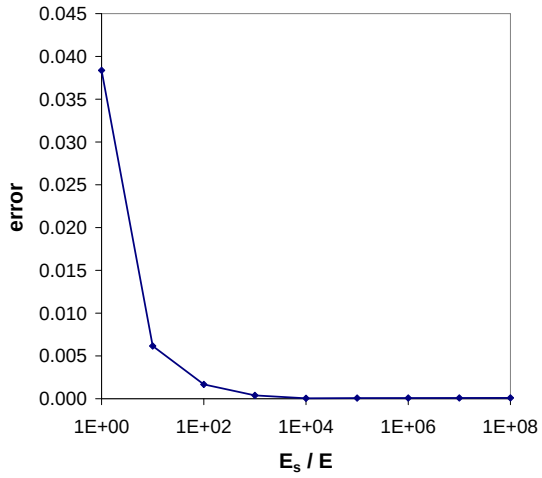

Figure 29: V-shaped arch. Relative angle change as a function of the bending strip stiffness.

The computation is done for different bending strip stiffness values and the relative change of angle between patches is monitored. In this case, the angle is measured at ten equally distributed sampling points on each patch interface, and the maximum error is plotted in Figure 29. Note that for $E_s/E \geq 10^3$ the maximum relative error is less than 10^{-3}.

7.4. Hemispherical shell

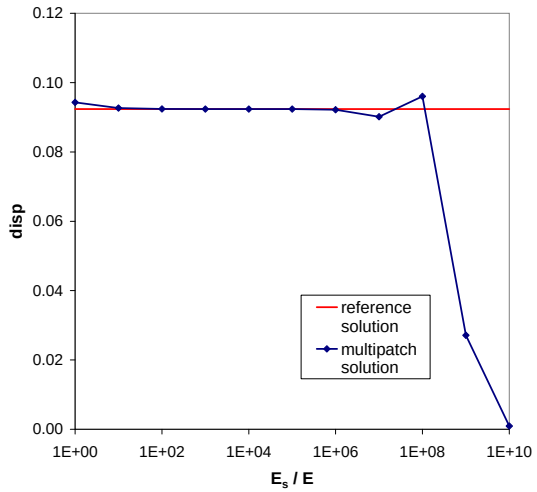

Figure 30: Pinched hemisphere. Displacement under the point load as a function of the bending strip stiffness.

Different bending strip stiffness values are also studied on the hemishperical shell example with the polynomial degree of the shell fixed at $p = 4$. In this problem there are significant differences in the element sizes (small elements at the pole and large elements at the rim of the hemisphere), which negatively affect the

conditioning of the stiffness matrix. The high bending strip stiffness is expected to increase the condition number of the stiffness matrix further, leading to a narrower range of stiffness ratios for which the solution is accurate and stable. This effect can be observed in Figure 30. For $10^2 \leq E_s/E \leq 10^5$ the reference solution is obtained. But for ratios $E_s/E \geq 10^6$ the stiffness matrix is badly conditioned and the solution becomes unstable.

The above examples indicate that, for problems where the load carrying behavior at the patch interface is dominated by bending, it is important to choose the bending strip stiffness values to be not too low. On the other hand, choosing a too high stiffness value may lead to numerical problems caused by bad conditioning of the equation system. For all problems presented in this paper, the bending strip stiffness in the range of $10^3 \leq E_s/E \leq 10^5$ yields reliable and stable results.

8. Conclusions

A new bending strip method is presented to handle multi-patch isogeometric discretization of the rotation-free Kirchhoff-Love shells. The method is efficient, simple to implement, and is applicable to a large class of multi-patch shell geometries. G^1-continuous patch intersections as well as patches meeting at a kink are handled in a unified manner. The bending strip approach was tested on a set of well-known benchmark examples, both in the linear and geometrically non-linear regime, and very good results were obtained in all cases. An application to a wind turbine rotor subjected to wind loads coming from a separate fluid mechanics computation is also shown. The method is further extended to the coupling of shells and solids, for which accurate numerical results are attained.

9. Acknowledgement

The authors would like to acknowledge the funding of the International Graduate School of Science and Engineering (IGSSE) at Technische Universität München, which is part of the German Excellence Initiative.

[1] J. Kiendl, K.-U. Bletzinger, J. Linhard, and R. Wüchner. Isogeometric shell analysis with Kirchhoff–Love elements. *Computer Methods in Applied Mechanics and Engineering*, 198:3902–3914, 2009.

[2] T.J.R. Hughes, J.A. Cottrell, and Y. Bazilevs. Isogeometric analysis: CAD, finite elements, NURBS, exact geometry and mesh refinement. *Computer Methods in Applied Mechanics and Engineering*, 194:4135–4195, 2005.

[3] Y. Bazilevs, V.M. Calo, T.J.R. Hughes, and Y. Zhang. Isogeometric fluid-structure interaction: theory, algorithms, and computations. *Computational Mechanics*, 43:3–37, 2008.

[4] Y. Bazilevs, J.R. Gohean, T.J.R. Hughes, R.D. Moser, and Y. Zhang. Patient-specific isogeometric fluid-structure interaction analysis of thoracic aortic blood flow due to implantation of the Jarvik 2000 left ventricular assist device. *Computer Methods in Applied Mechanics and Engineering*, 198:3534–3550, 2009.

[5] Y. Bazilevs and T.J.R. Hughes. NURBS-based isogeometric analysis for the computation of flows about rotating components. *Computational Mechanics*, 43:143–150, 2008.

[6] J.G. Isaksen, Y. Bazilevs, T. Kvamsdal, Y. Zhang, J.H. Kaspersen, K. Waterloo, B. Romner, and T. Ingebrigtsen. Determination of wall tension in cerebral artery aneurysms by numerical simulation. *Stroke*, 39:3172–3178, 2008.

[7] M.-C. Hsu, Y. Bazilevs, V.M. Calo, T.E. Tezduyar, and T.J.R. Hughes. Improving stability of stabilized and multiscale formulations in flow simulations at small time steps. *Computer Methods in Applied Mechanics and Engineering*, 199:828–840, 2010.

[8] Y. Bazilevs, V.M. Calo, J.A. Cottrel, T.J.R. Hughes, A. Reali, and G. Scovazzi. Variational multiscale residual-based turbulence modeling for large eddy simulation of incompressible flows. *Computer Methods in Applied Mechanics and Engineering*, 197:173–201, 2007.

[9] Y. Bazilevs, C. Michler, V.M. Calo, and T.J.R. Hughes. Weak Dirichlet boundary conditions for wall-bounded turbulent flows. *Computer Methods in Applied Mechanics and Engineering*, 196:4853–4862, 2007.

[10] Y. Bazilevs, C. Michler, V.M. Calo, and T.J.R. Hughes. Isogeometric variational multiscale modeling of wall-bounded turbulent flows with weakly-enforced boundary conditions on unstretched meshes. *Computer Methods in Applied Mechanics and Engineering*, 199:780–790, 2008.

[11] T. Elguedj, Y. Bazilevs, V.M. Calo, and T.J.R. Hughes. $\overline{\mathrm{B}}$ and $\overline{\mathrm{F}}$ projection methods for nearly incompressible linear and non-linear elasticity and plasticity using higher-order NURBS elements. *Computer Methods in Applied Mechanics and Engineering*, 197:2732–2762, 2008.

[12] I. Akkerman, Y. Bazilevs, V.M. Calo, T.J.R. Hughes, and S. Hulshoff. The role of continuity in residual-based variational multiscale modeling of turbulence. *Computational Mechanics*, 41:371–378, 2008.

[13] Y. Bazilevs, V.M. Calo, T.E. Tezduyar, and T.J.R. Hughes. *YZβ* discontinuity capturing for advection-dominated processes with application to arterial drug delivery. *International Journal for Numerical Methods in Fluids*, 54:593–608, 2007.

[14] J.A. Cottrell, A. Reali, Y. Bazilevs, and T.J.R. Hughes. Isogeometric analysis of structural vibrations. *Computer Methods in Applied Mechanics and Engineering*, 195:5257–5296, 2006.

[15] Y. Zhang, Y. Bazilevs, S. Goswami, C. Bajaj, and T.J.R. Hughes. Patient-specific vascular NURBS modeling for isogeometric analysis of blood flow. *Computer Methods in Applied Mechanics and Engineering*, 196:2943–2959, 2007.

[16] Y. Bazilevs, V.M. Calo, Y. Zhang, and T.J.R. Hughes. Isogeometric fluid-structure interaction analysis with applications to arterial blood flow. *Computational Mechanics*, 38:310–322, 2006.

[17] H. Gómez, V.M. Calo, Y. Bazilevs, and T.J.R. Hughes. Isogeometric analysis of the Cahn-Hilliard phase-field model. *Computer Methods in Applied Mechanics and Engineering*, 197:4333–4352, 2008.

[18] W.A. Wall, M.A. Frenzel, and C. Cyron. Isogeometric structural shape optimization. *Computer Methods in Applied Mechanics and Engineering*, 197:2976–2988, 2008.

[19] Y. Bazilevs and I. Akkerman. Large eddy simulation of turbulent Taylor–Couette flow using isogeometric analysis and the residual–based variational multiscale method. *Journal of Computational Physics*, 229:3402–3414, 2010.

[20] Y. Bazilevs, L. Beirao da Veiga, J.A. Cottrell, T.J.R. Hughes, and G. Sangalli. Isogeometric analysis: Approximation, stability and error estimates for h-refined meshes. *Mathematical Models and Methods in Applied Sciences*, 16:1031–1090, 2006.

[21] J.A. Evans, Y. Bazilevs, I. Babuška, and T.J.R. Hughes. n-Widths, sup-infs, and optimality ratios for the k-version of the isogeometric finite element method. *Computer Methods in Applied Mechanics and Engineering*, 198:1726–1741, 2009.

[22] D.J. Benson, Y. Bazilevs, M.C. Hsu, and T.J.R. Hughes. Isogeometric shell analysis: The Reissner–Mindlin shell. *Computer Methods in Applied Mechanics and Engineering*, 199:276–289, 2010.

[23] D.J. Benson, Y. Bazilevs, E. De Luycker, M.-C. Hsu, M. Scott, T.J.R. Hughes, and T. Belytschko. A generalized finite element formulation for arbitrary basis functions: from isogeometric analysis to XFEM. *International Journal for Numerical Methods in Engineering*, 2010. Accepted.

[24] V. Srinivasan, S. Radhakrishnan, and G. Subbarayan. Coordinated synthesis of hierarchical engineering systems. *Computer Methods in Applied Mechanics and Engineering*, 199:392–404, 2010.

[25] S. Lipton, J.A. Evans, Y. Bazilevs, T. Elguedj, and T.J.R. Hughes. Robustness of isogeometric structural discretizations under severe mesh distortion. *Computer Methods in Applied Mechanics and Engineering*, 199:357–373, 2010.

[26] W. Wang and Y. Zhang. Wavelets-based NURBS simplification and fairing. *Computer Methods in Applied Mechanics and Engineering*, 199:290–300, 2010.

[27] E. Cohen, T. Martin, R.M. Kirby, T. Lyche, and R.F. Riesenfeld. Analysis-aware modeling: Understanding quality considerations in modeling for isogeometric analysis. *Computer Methods in Applied Mechanics and Engineering*, 199:334–356, 2010.

[28] F. Auricchio, L. Beirão da Veiga, C. Lovadina, and A. Reali. The importance of the exact satisfaction of the incompressibility constraint in nonlinear elasticity: Mixed FEMs versus NURBS-based approximations. *Computer Methods in Applied Mechanics and Engineering*, 199:314–323, 2010.

[29] Y. Bazilevs, V.M. Calo, J.A. Cottrell, J.A. Evans, T.J.R. Hughes, S. Lipton, M.A. Scott, and T.W. Sederberg. Isogeometric analysis using T-splines. *Computer Methods in Applied Mechanics and Engineering*, 199:264–275, 2010.

[30] M.R. Dörfel, B. Jüttler, and B. Simeon. Adaptive isogeometric analysis by local *h*-refinement with T-splines. *Computer Methods in Applied Mechanics and Engineering*, 199:264–275, 2010.

[31] M. Bischoff, W.A. Wall, K.-U. Bletzinger, and E. Ramm. Models and finite elements for thin-walled structures. In E. Stein, R. de Borst, and T.J.R. Hughes, editors, *Encyclopedia of Computational Mechanics, Vol. 2, Solids, Structures and Coupled Problems*, chapter 3. Wiley, 2004.

[32] K.-U. Bletzinger, M. Firl, J. Linhard, and R. Wüchner. Optimal shapes of mechanically motivated surfaces. *Computer Methods in Applied Mechanics and Engineering*, 199:324–333, 2010.

[33] K.-U. Bletzinger, R. Wüchner, F. Daoud, and N. Camprubí. Computational methods for form finding and optimization of shells and membranes. *Computer Methods in Applied Mechanics and Engineering*, 194:3438–3452, 2005.

[34] E. Oñate and F. Zárate. Rotation-free triangular plate and shell elements. *International Journal for Numerical Methods in Engineering*, 47:557–603, 2000.

[35] F. Cirak and M. Ortiz. Fully C^1-conforming subdivision elements for finite deformation thin–shell analysis. *International Journal for Numerical Methods in Engineering*, 51:813–833, 2001.

[36] J. Linhard, R. Wüchner, and K.-U. Bletzinger. "Upgrading" membranes to shells–The CEG rotation free shell element and its application in structural analysis. *Finite Elements in Analysis and Design*, 44:63–74, 2007.

[37] K.-U. Bletzinger, S. Kimmich, and E. Ramm. Efficient modeling in shape optimal design. *Computing Systems in Engineering*, 2:483–495, 1991.

[38] T. Belytschko, W.K. Liu, and B. Moran. *Nonlinear Finite Elements for Continua and Structures*. Wiley, 2000.

[39] D.F. Rogers. *An Introduction to NURBS With Historical Perspective*. Academic Press, San Diego, CA, 2001.

[40] J.A. Cottrell, T.J.R. Hughes, and Y. Bazilevs. *Isogeometric Analysis: Toward Integration of CAD and FEA*. John Wiley & Sons, Ltd, New York, NY, 2009.

[41] T. Belytschko, H. Stolarski, W.K. Liu, N. Carpenter, and J.S.-J. Ong. Stress projection for membrane and shear locking in shell finite elements. *Computer Methods in Applied Mechanics and Engineering*, 51:221–258, 1985.

[42] J. Jonkman, S. Butterfield, W. Musial, and G. Scott. Definition of a 5-MW reference wind turbine for offshore system development. Technical Report NREL/TP-500-38060, National Renewable Energy Laboratory, Golden, CO, 2009.

[43] Y. Bazilevs, M.-C. Hsu, D.J Benson, and T.E. Tezduyar. Computational fluid-structure interaction for wind energy applications. In *Proceedings of the III International Conference on Computational Methods in Marine Engineering (MARINE 2009)*, Trondheim, Norway, June 2009.

[44] I.M. Daniel and O. Ishai. *Engineering Mechanics of Composite Materials, 2nd ed.* Oxford University Press, New York, NY, 2005.

[45] E. Rank, A. Düster, V. Nübel, K. Preusch, and O.T. Bruhns. High order finite elements for shells. *Computer Methods in Applied Mechanics and Engineering*, 194:2494–2512, 2004.

[46] Rhino. NURBS modeling for Windows. http://www.rhino3d.com/.

[47] R. Schmidt. *Development and Implementation of a Rhino Preprocessor for the Integration of CAD and Isogeometric Analysis*. Master's thesis, Technische Universität München, 2009.